Yun Zhou[1], Lisheng Xu[1], Zhengyang Pan[2], Ming Hao[3], and Chunlai Li[1]

[1]Institute of Geophysics, China Earthquake Administration, Beijing 100081, China

[2]Institute of Earthquake Forecasting, China Earthquake Administration, Beijing 100036, China

[3]The Second Monitoring and Application Center, China Earthquake Administration, Xi'an 710054, China

Corresponding author: Lisheng Xu (xuls@cea-igp.ac.cn)

Key Points:

- The 1733DC-M7.8 earthquake has occupied an asperity locked much more than the 1833SM-M8.0 earthquake
- The local deformation and seismicity associated with the locked asperity are characterized by the near-fault GNSS and seismic observations
- A typical example is presented as evidence supporting the freshly proposed model for generation of large earthquake (Kato & Ben-Zion, 2021)

Abstract

As early as in 1733, an M~7.8 earthquake (1733DC-M7.8 earthquake) ruptured the 110km-long northern segment of the Xiaojiang fault zone, on the southeastern boundary of Tibetan plateau, and 100 years later, in 1833, another M~8.0 earthquake (1833SM-M8.0 earthquake) broke the 130 km-long middle segment. Here we show a new insight into the source of the 1733DC-M7.8 earthquake through the latest regional GNSS measurements plus our near-fault seismic and GNSS observations since February 2012. An inversion of the regional GNSS measurements resolved an asperity for the 1733DC-M7.8 earthquake that is bearing more slip deficit in comparison with the 1833SM-M8.0 earthquake, implying an Mw7.2+ earthquake, and the near-fault GNSS and seismic observations not only justified this asperity with localized deformation and multi-scaled seismicity but also are declaring an impending rupture of the asperity. More importantly, this work contributes a typical example to the recently proposed model for the generation of large earthquakes.

Plain Language Summary

Once two disastrous earthquakes struck the southeastern boundary of Tibetan plateau since historically recorded. One occurred on the northern section of the Xiaojiang fault zone in 1733, with a magnitude of M7.8, and the other took place on the middle section in 1833, with a magnitude of M8.0. Whether a new large earthquake will come out to rupture these old faults has become one of the important things that seismologists are caring about. Therefore, we specially conducted dense seismic plus GNSS near-fault observations across the northern section of the Xiaojiang fault zone. Here we presented a newest investigation of the source region of the two historical earthquakes based on

our near-fault observation data and the latest regional GNSS data. As the investigation showed, at least an Mw7.2 earthquake is getting ready, and to burst probably soon just in the place of the M7.8 historical earthquake.

1 Introduction

The collision and continued convergence of the India and Eurasia blocks resulted in the rapid uplift of the Tibetan Plateau. During strong orogenic activity, the motion of large-scale faults has been ongoing together with lateral extrusion of huge entity (Molnar & Tapponnier, 1975; Rowley, 1996). The Xianshuihe (XSHF)-Anninghe (ANF)-Zemuhe (ZMF)-Xiaojiang (XJF) fault system is one of such large-scale faults, which outlines the southeastern boundary of the Tibetan plateau (Fig. 1) (Allen et al., 1984; Tapponnier & Molnar, 1977). This boundary has been playing a crucial role in accommodating the uplift and expansion of the Tibetan Plateau (Hu et al., 2012; Xu et al., 2003), and generated tens of disastrous earthquakes in history (P. Li, 1993; Song et al., 1998).

The XJF is the southernmost section of the southeastern boundary of Tibetan plateau, along which more than 10 middle-to-large size earthquakes have occurred since 1500 (Fig. 1; Table S1). The most disastrous should be the M7.8 event, which occurred in Dongchuan county, Yunnan province, in 1733 (the 1733DC-M7.8 earthquake), and the M8.0 event, which took place in Songming county, Yunnan province, in 1833 (the 1833SM-M8.0 earthquake). The 1733DC-M7.8 earthquake ruptured approximately 110km-long ground surface on the northern section of the XJF (Fig. S1), which caused collapse of mine caves and killed more than 10000 people (Cui, 1735; Y. Wang et al., 2017). The 1833SM-M8.0 earthquake ruptured approximately 130km-long ground surface on the middle section of the XJF (Fig. S1), which caused more than 6700 deaths and injured 5000 people as estimated (J. Li et al., 2021). Afterwards, no earthquakes larger than M7.0 appeared on the northern and middle sections, so the seismic risk of the XJF has drawn strong attention.

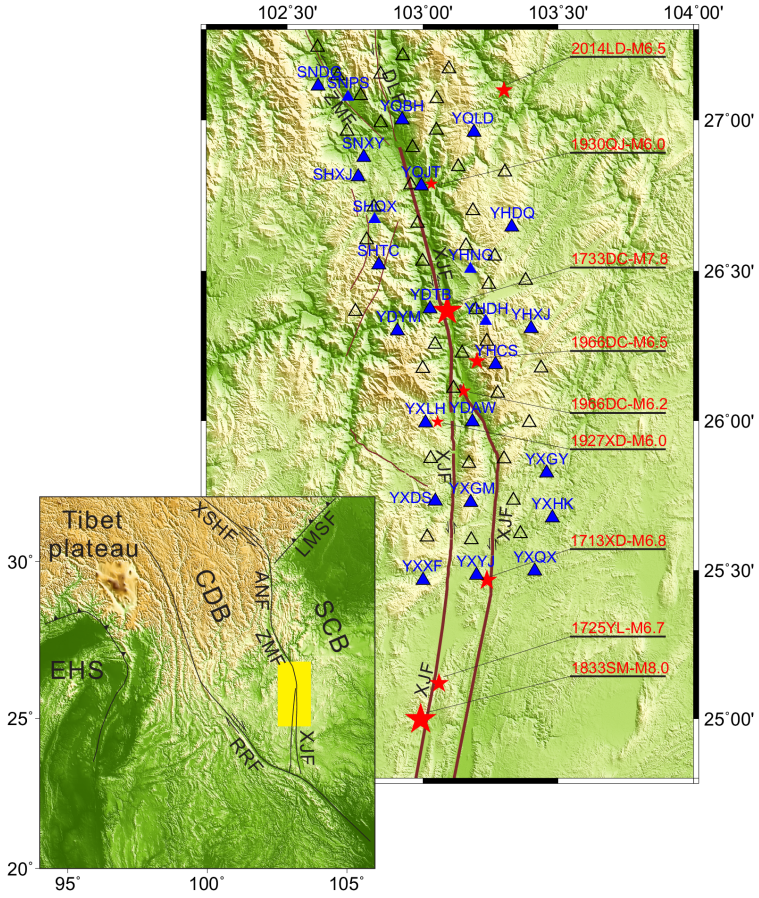

Figure 1. Distribution of the GNSS stations (blue triangles) and seismic stations (black empty triangles) in the north and central sections of Xiaojiang fault (XJF). Brown solid lines emphasize the XJF, and the red stars denote the M>6 historical earthquakes since 1500. The subplot in the lower left corner shows the area of the main plot (yellow rectangle) with respect to the Chuandian Block (CDB) and the South China Block (SCB). Abbreviations: XSHF, Xianshuihe fault; ANF, Anninghe fault; ZMF, Zemuhe fault; XJF, Xiaojiang fault; DLF, Daliangshan fault; LMSF, Longmenshan fault; RRF, Red River fault; SCB, South China block; CDB, Chuandian block; EHS, Eastern Himalayan Syntaxis. Abbreviations in earthquake names: LD, Ludian; QJ, Qiaojia; DC, Dongchuan;

XD, Xundian; YL, Yiliang; SM, Songming.

In fact, the potential seismic risk on the XJF had been studied (Liu et al., 2020; Mao et al., 2016; F. Wang et al., 2015; Wen et al., 2008; Yi et al., 2008). Wen et al. (2008) concluded that one seismic gap was on the northern segment of the XJF while another was at the southernmost tip after analyzing a variety of data, especially including the spatial distributions of historical earthquakes and their rupture dimensions together with the spatial patterns of modern earthquakes. F. Wang et al. (2015) suggested that the northern section of the XJF had prepared the capacity generating an Mw7.6 earthquake after estimating the accumulation of the elastic strain by comparing the accumulation rates of seismic moment calculated with GNSS-velocity data and the seismic moment already released in the past. Recently, Liu et al. (2020) also claimed that a large earthquake was about to visit the whole mid-northern segment of the XJF after analyzing the activity of historical earthquakes and the seismicity of recent decades. Anyhow, the probability of disastrous earthquakes occurring on the XJF, especially on its northern segment, is arising.

However, the previous studies were lack of near-fault observations, which might have produced low-resolution or even fake images on seismic risk. In order to understand the behavior of the northern segment of the XJF, we started to deploy a GNSS and seismic array (Fig. 1) as early as February of 2012, and kept it in operation till now. In this study, we employed our near-fault observations to focus on the source zones of the 1733DC-M7.8 earthquake, which is entirely covered by our array, together with the latest regional GNSS measurements (M. Wang & Shen, 2020).

2 Near-fault and regional GNSS data

Our GNSS stations were equipped with the TOPCON NET-G3A and NET-G5 receivers plus CR-G3 and CR-G5 antennas. The instruments were powered by solar panels and kept in continuous operation at a sampling rate of 30s. The data was processed with the GAMIT/GLOBK software developed by the Massachusetts Institute of Technology (Herring et al., 2015) as we did in our previous work (Zhou et al., 2016). The co-seismic effect of the 2014 Ms6.5 Ludian earthquake, which occurred near our observational area (Fig. 1), was removed when we calculated the velocities of observation points.

We collected the latest data of the regional GNSS velocity field for the XJF and its surrounding region (M. Wang & Shen, 2020), and combined it with our near-fault data (see Data Availability Statement) in the Eurasian frame (Fig. 2) by means of the VELROT program (Herring et al., 2015). As Fig. 2a shows, our near-fault GNSS observations contributed more velocity vectors which are similar in direction to previous investigations. Apparently, our near-fault GNSS observations obviously increased the density of observed velocity vectors. This combined dataset was fundamentally essential for investigation of the XJF behavior.

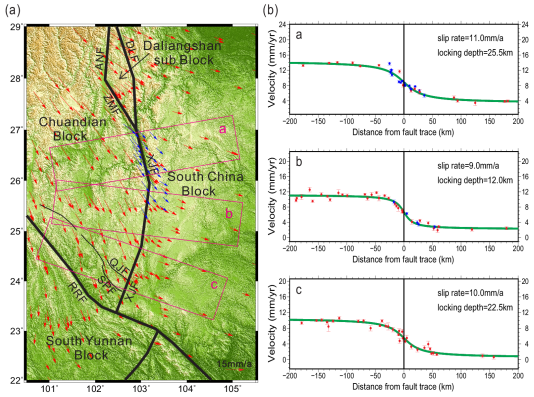

Figure 2. GNSS velocity field, the block models used in inversion (a) and the Savage-fittings along the profiles (b). In panel (a), red velocity vectors are from the newest study (M. Wang & Shen, 2020) and the blue velocity vectors are from our near-fault observations. The black thick solid lines indicate the block boundaries or major faults. Purple rectangles show the GNSS profiles. Abbreviations: QJF, Qujiang fault; SPF, Shiping fault. In panel (b), the green curves are from the Savage-fitting; panels a, b and c correspond to the profiles a, b and c across the northern, middle and south sections of the XJF, respectively.

3 Fitting for the slip rates and locking depths of the XJF

The combined dataset allowed us to investigate the slip rates and locking depths of the XJF by means of the traditional method (Savage et al., 1999) (Savage-Fitting) described as

(1)

where and are the distance from observation point to fault trace and the velocity component parallel to the fault plane observed at the observation point, respectively, and and are the slip rate and the locking depth of the fault, respectively. We designed three profiles for the northern, middle and southern sections, respectively, in accordance with the trends of the different sections (Fig. 2). The best fitting led to a slip rate of 11mm/a and a locking depth of 25.5km for the

northern section, a slip rate of 9mm/a and a locking depth of 12km for the middle section, and a slip rate of 10mm/a and a locking depth of 22.5km for the southern section. A comparison of the slip rates and the locking depths among the three sections clearly shows that the middle section has a much shallower locking depth though the slip rates on the three sections appeared to be comparable. It should be stressed that not only regional data but also the near-fault data are fitted very well on the northern and middle sections (Fig. 2a and 2b).

4 Inversion for the locking ratio heterogeneity on the XJF

Following other studies (Loveless & Meade, 2011; W. Wang et al., 2017), we constructed a model, which consists of the Chuandian, South China, South Yunnan blocks and the Daliangshan sub-block (Fig. 2a), and inverted the regional GNSS data for the present slip heterogeneity of the XJF using the DEFNODE program (McCaffrey et al., 2007; McCaffrey et al., 2002). We had to stress that the XJF was simplified into a single fault due to the resolution of observations as well as the convenience of inversion though it separates into two branches in the middle and southern sections (Fig. 1), and that the near-fault GNSS data was not employed because of its sensitivity to geometrical complexity of the fault. The fault plane was gridded into 2km×2km units, and initially given to be fully locked above depth of 15km, to be completely free below 25km, and to have locking ratios decreasing smoothly from 15km to 25km. The best solution was achieved when the reduced chi-square value (Pan et al., 2021) reached the minimum.

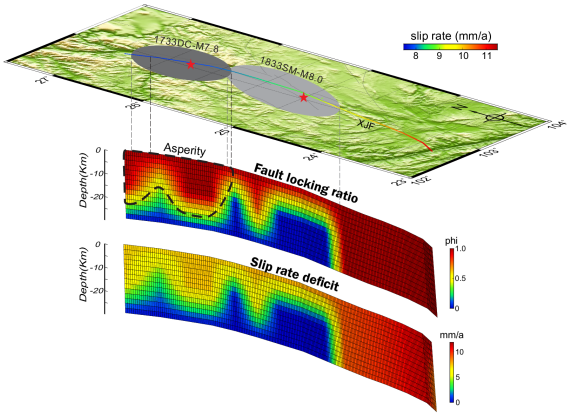

Figure 3. Image of the inverted slip rate (top), locking ratio (middle) and slip-rate deficit (bottom) of the XJF. The epicenters and rupture sites of the 1733DC-M7.8 and the 1833SM-M8.0 earthquakes (Wen et al., 2008) are marked with the red stars and gray (dark and white) colors, respectively. The source fault of the 1733DC-M7.8 earthquake is emphasized with the dashed black curve for it has been locked much more than the 1833SM-M8.0 earthquake and thus was focused on in this study.

After a number of the performances with various parameters (Table S2, Figs. S2-S13) (Jiang et al., 2015; J. Li et al., 2020; Y. Wang et al., 2014; B. Zhang et al., 2008; Zhao et al., 2014) and comparison of their residual distributions (Fig. S14), we chose the model as shown in Fig. 3 because it best explained the observed data (Fig. S13 and Fig. S14). It was stressed that the locations of the boundaries were adjusted while the dipping angles and directions were tried (Fig. S15). Comparing the fault locking ratio inverted (Fig. 3), we found an interesting coincidence that the 1733DC-M7.8 earthquake occupied a segment of fault locked much more than the 1833SM-M8.0 earthquake, which should be attributed to the difference of 100 years between the two events.

We noticed that all the inverted models failed to avoid the larger residuals

distributed in the southeastern corner of the Chuandian block due to the nappe structure there (Wen et al., 2011) and the boundary effect of the inversion model, so this study did not pay attention to the southern segment of the XJF. Instead, we specially focused on the northern section of the XJF where the 1733DC-M7.8 earthquake occurred because of the perfect coverage of our near-fault GNSS and seismic array (Fig. 1).

As the above inversion revealed (Fig. 3), a large percentage of the northern section had been locked above the depth of 24km, especially 18km in spite of the locking-ratio heterogeneity, which was obviously different from the middle section where the 1833SM-M8.0 earthquake occurred. This difference was also supported by the Savage-fitting in the section 3 (Fig. 2b and Fig. 2c). In addition, we noticed that a similar locked asperity was exhibited in a recent study (Fig. S16) (Y. Li et al., 2021) though it was relatively larger in size, covering the northern plus middle sections, perhaps due to the resolution and other sources.

Furthermore, we estimated a magnitude for the potential earthquake defined with the asperity as outlined in the Fig. 3 based on to its geometries and slip rate deficit (Kanamori, 1977, 1994). Our estimation suggested that the potential earthquake would reach at least Mw7.2.

5 Deformation of the ground surface

Spatial distribution of strain-rate tensors usually used to describe the heterogeneity of ground surface deformation, so we adopted the traditional method (Hackl et al., 2009; Wessel & Bercovici, 1998) to construct a spatial distribution of strain-rate tensors for the blocks involved (Fig. S17) based on the combined GNSS dataset. The spatial pattern showed that large strain rates appeared along the major faults, dominant shear strain distributed along the major strike-slip faults (Fig. S17), and the principal axes of the tensors displayed a clockwise rotation from north to south along the ANF-ZMF-XJF. All these characteristics were in a good agreement with those revealed by previous studies (Gan et al., 2007; M. Wang & Shen, 2020; P. Zhang et al., 2004).

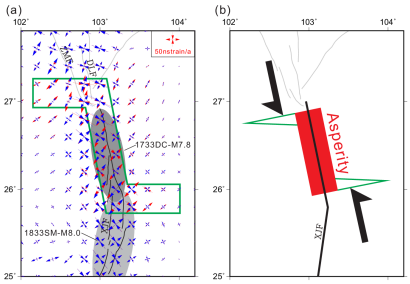

Figure 4. The spatial pattern of the strain-rate tensors from the regional GNSS observations only (blue) and the combination of the regional and our near-fault GNSS observations (red). (a) The Z-shaped deformation (green Z-shape) revealed by the comparison of the strain-rate tensors from the two types of datasets. (b) A conceptual model proposed to understand the Z-shaped deformation as exhibited in subplot (a). The red filled box represents the locked asperity, the two green wings show the obviously deformed areas at the two tips of the locked asperity, and a pair of large black arrows indicates the driving force to the locked asperity due to the left-lateral strike slip of the XJF(Also see Figs. 2 and 3 for more).

However, an obvious and robust difference stood out across our near-fault observational area (Fig. 4) as we compared the spatial patterns of strain-rate tensors from the combined dataset (Fig. S17) and the single regional GNSS data (Fig. S18). This difference clearly indicated an evidential contribution of our near-fault observation! In particular, the largest differences in the principal compressive and extensive strain rate reached 117% and 54%, respectively, and the maximum alteration in the direction of principle axis was up to 15°. With our near-fault GNSS observations, the deformation heterogeneity of the observational region was clearly characterized with a Z-shaped area.

Here we had to stress that the Z-shaped deformation was closely related with the locked asperity (Fig. 4a). Our near-fault GNSS stations were NOT deployed within a Z-shaped area (Fig. 1), instead, were nearly normally distributed in

the entire northern part! To explain the Z-shaped deformation, we proposed a conceptual model (Fig. 4b). As Fig. 4b illustrates, the locked asperity kept the northern section of the XJF from stable slipping under the drive of the left-lateral creep-slipping plus sticky slipping in the lower crust and deeper, so that the deformation took place near ground surface along and at two tips of the locked asperity. Thus, the Z-shaped deformation was an important evidence supporting the locked asperity.

6 Near-fault seismicity

Together with the near-fault GNSS array, we deployed a seismic array in the same area (Fig. 1, 5a). The seismic array were composed of 61 stations, but the southern half of the array started in November 2018. Fig. 5a shows the stations which have not only been in operation since February of 2012 but also completely covered the northern section of the XJF. This array was able to locate seismic events of ML-0.7, but most of the located events had magnitudes ranging from ML0.0 to ML2.0.

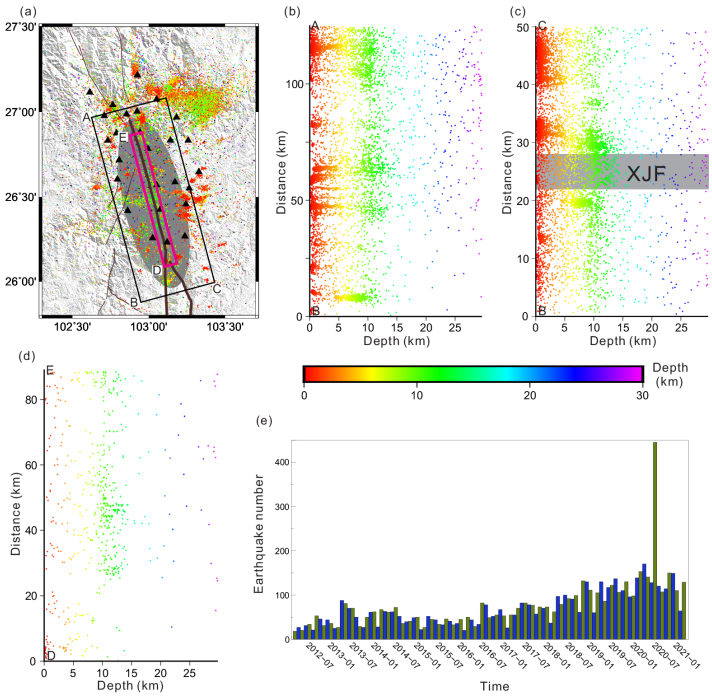

Figure 5. The clusters and swarms of the seismicity in the volume surrounding the locked asperity. (a) The M<2 earthquakes (small circles) recorded by our near-fault seismic stations (black triangles) in the period of February 2012 to March 2021. The 50km-wide black frame surrounds the entire locked asperity whereas the 6km-wide purple frame merely surrounds the central part. (b) The seismicity in the larger frame projected on the cross-section parallel to the fault plane (see side A-B in Fig. 5a). (c) The seismicity in the larger frame projected on the cross-section perpendicular to the fault plane (see side B-C in Fig. 5a). (d) The seismicity in the smaller frame projected on the cross-section parallel to the fault plane (see side D-E in Fig. 5a). (e) The monthly counts of the earthquakes shallower than 18km in the larger frame in the period of February 2012 to March 2021.

From February 2012 to March 2021, a total of 21653 micro-earthquakes were located across the observational region (Fig. 5a), but only a small percentage of the events took place along the XJF. As Fig. 5a shows, there were 8467 events (39.1%) within the large frame whose eastern and western sides are 25km distant from the fault plane, and there are only 603 events (2.8%) distributed within the small frame whose eastern and western sides are only 3 km distant from the fault plane. These characteristics were closely related with the off-fault deformation due to the locked asperity.

As the cross-sections parallel and perpendicular to the fault (Figs. 5b, 5c and 5d) show, only a small percentage of the events occurred on the central part of and with a narrow zone near the locked asperity, and an absolutely large percentage of the events were distributed above the depth of 18km, that is, in the interior of seismogenic zone. In addition, a relatively large percentage of the near-fault events took place in the middle depth of the locked asperity (Figs. 5a and 5d), where sticky slipping might occur more easily.

Base on the fact that a large percentage of the events occurred off the fault plane of the locked asperity, we analyzed the time-dependent seismicity within the zone framed with the large rectangle (Fig. 5a). As Fig. 5e shows, the monthly counts of the micro-earthquakes have been increasing since our array started, and more rapidly recent years. Such a rapidly increasing trend indicated that the observational region around the locked asperity is being loaded very quickly, implying that the rupture of the locked asperity is likely impending soon.

7 Discussions and conclusions

A locked asperity, corresponding to the source fault of the 1733DC-M7.8 earthquake, was identified by the latest regional GNSS measurements, a featured deformation of the ground surface above the locked asperity was revealed by the near-fault GNSS observations, and a characterized seismicity in the volume surrounding the locked asperity was exhibited by the near-fault seismic observations. Neither the seismicity characteristics nor the deformation feature could be explained by any of the traditional models, the pre-slip model or the cascade-up model, which always limits the seismicity or the deformation into a narrow space along the fault plane (Ellsworth & Bulut, 2018; Tape et al., 2018).

However, a new integrated model recently proposed by Kato and Ben-Zion (2021) offered an excellent explanation for both of the deformation feature and the seismicity characteristics. This model describes a process of the progressive localization from distributed failures in a rock volume enclosing potential large earthquake to localized deformation culminating in the generation of primary slip zones and large earthquakes, during which clusters or swarms of micro-earthquakes take place in multiple-scale faults in the vicinity of potential large earthquake. Essentially, the new model states that the initiation processes of large earthquakes are multi-scale and diverse, involving localization of deformation, fault heterogeneities and variable local loading rate effects. Therefore, the

pieces of the phenomenon discovered by our near-fault GNSS and seismic array are easily understandable.

In addition, as predicted by the integrated model for the generation of large earthquakes, a step-like increase that might reflect stress loading by previous failure may appear before the occurrences of larger slips or earthquakes (Kato & Ben-Zion, 2021). As shown in the Fig. 5e, the monthly counts of the micro-earthquakes around the locked asperity display a progressively increasing trend. Perhaps, this increasing is an important indicator of culminating stress loading.

Altogether, our work presented here may be concluded as the following: (1) the source fault of the 1733DC-M7.8 earthquake has been locked or at least locked much more than that of the 1833SM-M8.0 earthquake; (2) the locked asperity might evolve into an Mw7.2+ earthquake soon; (3) near-fault GNSS and seismic observations can certainly play an important role in monitoring the pre-processes of large earthquakes by revealing the local deformation and exhibiting the multi-scale seismicity associated with potential earthquakes; (4) our observations and research contributes a typical example as evidence supporting the freshly proposed model for the generation of large earthquakes (Kato & Ben-Zion, 2021).

Acknowledgments

We acknowledge the financial support from the National Natural Science Foundation of China (Project: 41904050, U2139205), and the Special Fund of the Institute of Geophysics, China Earthquake Administration (Grant Number: DQJB19B33). GMT software was used to create the figures and maps. The authors declare that they have no conflicts of interest.

Data Availability Statement

The near-fault GPS velocity dataset of this study are uploaded to the open-access repository Zenodo website for sharing purpose (https://doi.org/10.5281/zenodo.5829718). The GPS velocities used in block inversion can be obtained from https://doi.org/10.1029/2019JB018774 (Wang & Shen, 2020).

References

Allen, C., Gillespie, A., Yuan, H., Sieh, K. E., Buchun, Z., & Chengnan, Z. (1984). Red River and associated faults, Yunnan Province, China: Quaternary geology, slip rates, and seismic hazard. Geological Society of America Bulletin, 95(6), 686-700.

Cui, N. (1735). The earthquake chronicle in Dongchuan Prefecture (in Chinese).

Ellsworth, W. L., & Bulut, F. (2018). Nucleation of the 1999 Izmit earthquake by a triggered cascade of foreshocks. Nature Geoscience, 11(7), 531-535.

Gan, W., Zhang, P., Shen, Z., Niu, Z., Wang, M., Wan, Y., et al. (2007). Present-day crustal motion within the Tibetan Plateau inferred from GPS measurements. Journal of Geophysical Research: Solid Earth, 112(B8).

Hackl, M., Malservisi, R., & Wdowinski, S. (2009). Strain rate patterns from dense GPS networks. Natural Hazards and Earth System Sciences, 9(4), 1177-1187.

Herring, T., King, R., Floyd, M., & McClusky, S. (2015). GAMIT Reference Manual. GPS Analysis at MIT GLOBK, Release 10. 6. In: Massachusetts Institute of Technology.

Hu, J., Yang, H., Xu, X., Wen, L., & Li, G. (2012). Lithospheric structure and crust–mantle decoupling in the southeast edge of the Tibetan Plateau. Gondwana Research, 22(3-4), 1060-1067.

Jiang, G., Xu, X., Chen, G., Liu, Y., Fukahata, Y., Wang, H., et al. (2015). Geodetic imaging of potential seismogenic asperities on the Xianshuihe-Anninghe-Zemuhe fault system, southwest China, with a new 3-D viscoelastic interseismic coupling model. Journal of Geophysical Research: Solid Earth, 120(3), 1855-1873.

Kanamori, H. (1977). The energy release in great earthquakes. Journal of Geophysical Research, 82(20), 2981-2987.

Kanamori, H. (1994). Mechanics of earthquakes. Annual review of earth and planetary sciences, 22(1), 207-237.

Kato, A., & Ben-Zion, Y. (2021). The generation of large earthquakes. Nature Reviews Earth & Environment, 1-14.

Li, J., Böse, M., Feng, Y., & Yang, C. (2021). Real-Time Characterization of Finite Rupture and Its Implication for Earthquake Early Warning: Application of FinDer to Existing and Planned Stations in Southwest China. Front. Frontiers in Earth Science, 9, 699560.

Li, J., Zhou, B., Li, T., Yang, Y., Li, Z., & Long, F. (2020). Seismogenic depths of the Anninghe-Zemuhe and Daliangshan fault zones and their seismic hazards Chinese Journal of Geophysics. Chinese Journal of Geophysics(in Chinese), 63(10), 3669-3682.

Li, P. (1993). Xianshuihe-Xiaojiang Fault Zone: Beijing :Seismological Press (in Chinese).

Li, Y., Nocquet, J.-M., Shan, X., & Jian, H. (2021). Heterogeneous Interseismic Coupling Along the Xianshuihe-Xiaojiang Fault System, Eastern Tibet. Journal of Geophysical Research: Solid Earth, 126(11).

Liu, J., Zhang, L., & Du, Y. (2020). Seismic Hazard Assessment of the Mid-Northern Segment of Xiaojiang Fault Zone in Southwestern China Using Scenario Earthquakes. Bulletin of the Seismological Society of America, 110(3), 1191-1210.

Loveless, J. P., & Meade, B. J. (2011). Partitioning of localized and diffuse deformation in the Tibetan Plateau from joint inversions of geologic and geodetic observations. Earth and Planetary Science Letters, 303(1-2), 11-24.

Mao, Y., Liu, Z., Ye, J., & Li, Z. (2016). Analysis on strong earthquake risk of Xiaojiang fault zone. Journal of Seismological Research, 39(2), 213-217.

McCaffrey, R., Qamar, A. I., King, R. W., Wells, R., Khazaradze, G., Williams, C. A., et al. (2007). Fault locking, block rotation and crustal deformation in the Pacific Northwest. Geophysical Journal International, 169(3), 1315-1340.

McCaffrey, R., Stein, S., & Freymueller, J. (2002). Crustal block rotations and plate coupling. Plate Boundary Zones, Geodyn. Ser, 30, 101-122.

Molnar, P., & Tapponnier, P. (1975). Cenozoic tectonics of Asia: effects of a continental collision. Science, 189(4201), 419-426.

Pan, Z., Zhang, Z., Shao, Z., & Zhao, G. (2021). Block motions and strain partition on active faults in Northeast Tibet and their geodynamic implications. Terra Nova, 00, 1-8. https://doi.org/10.1111/ter.12520

Rowley, D. B. (1996). Age of initiation of collision between India and Asia: A review of stratigraphic data. Earth and Planetary Science Letters, 145(1-4), 1-13.

Savage, J., Svarc, J., & Prescott, W. (1999). Geodetic estimates of fault slip rates in the San Francisco Bay area. Journal of Geophysical Research: Solid Earth, 104(B3), 4995-5002.

Song, F., Wang, Y., Yu, W., Cao, Z., Shen, X., & Shen, J. (1998). Xiaojiang Active Faults: Seismological Press, Beijing.

Tape, C., Holtkamp, S., Silwal, V., Hawthorne, J., Kaneko, Y., Paul, A. J., et al. (2018). Earthquake nucleation and fault slip complexity in the lower crust of central Alaska. Nature Geoscience, 11(7), 536-541.

Tapponnier, P., & Molnar, P. (1977). Active faulting and tectonics in China. Journal of Geophysical Research, 82(20), 2905-2930.

Wang, F., Wang, M., Wang, Y., & Shen, Z. (2015). Earthquake potential of the Sichuan-Yunnan region, western China. Journal of Asian Earth Sciences, 107, 232-243.

Wang, M., & Shen, Z. (2020). Present-day crustal deformation of continental China derived from GPS and its tectonic implications. Journal of Geophysical Research: Solid Earth, 125(2), e2019JB018774.

Wang, W., Qiao, X., Yang, S., & Wang, D. (2017). Present-day velocity field and block kinematics of Tibetan Plateau from GPS measurements. Geophysical Journal International, 208(2), 1088-1102.

Wang, Y., Wang, F., Wang, M., Shen, Z., & Wan, Y. (2014). Coulomb Stress Change and Evolution Induced by the 2008 Wenchuan Earthquake and its De-

layed Triggering of the 2013 Mw 6.6 Lushan Earthquake. Seismological Research Letters, 85(1), 52-59.

Wang, Y., Zhang, X., Zhang, J., Yang, S., Han, L., & Yan, S. (2017). Seismic mountainous geo-hazard investigation of Dongchuan Ms7.8 earthquake in 1733. South-to-North Water Transfers and Water Science & Technology, 15(1), 138-144.

Wen, X., Fang, D., Long, F., Fan, J., & Zhu, H. (2011). Tectonic dynamics and correlation of major earthquake sequences of the Xiaojiang and Qujiang-Shiping fault systems, Yunnan, China. Science China Earth Sciences, 054(10), 1563-1575.

Wen, X., Ma, S., Xu, X., & He, Y. (2008). Historical pattern and behavior of earthquake ruptures along the eastern boundary of the Sichuan-Yunnan faulted-block, southwestern China. Physics of the Earth and Planetary Interiors, 168(1-2), 16-36.

Wessel, P., & Bercovici, D. (1998). Interpolation with Splines in Tension: A Green's Function Approach. Mathematical Geology, 30(1), 77-93.

Xu, X., Wen, X., Zheng, R., Ma, W., Song, F., & Yu, G. (2003). Pattern of latest tectonic motion and its dynamics for active blocks in Sichuan-Yunnan region, China. Science in China Series D: Earth Sciences, 46(2), 210-226. journal article. https://doi.org/10.1360/03dz0017

Yi, G., Wen, X., & Su, Y. (2008). Study on the potential strong-earthquake risk for the eastern boundary of the Sichuan-Yunnan active faulted-block, China. Chinese Journal of Geophysics, 51(6), 1151-1158.

Zhang, B., Liu, R., Xiang, H., Wan, J., & Huang, X. (2008). Tectonite features and stress field variations associated with fault motion transformation in the central southern part of the Red River fault zone. Acta Petrologica Et Mineralogica, 27(6), 529-537.

Zhang, P., Shen, Z., Wang, M., Gan, W., Bürgmann, R., Molnar, P., et al. (2004). Continuous deformation of the Tibetan Plateau from global positioning system data. Geology, 32(9), 809-812.

Zhao, J., Liu, J., Niu, A., & Yan, W. (2014). Study on fault locking characteristic around the Daliangshan sub-block. Seismology and Geology(in Chinese), 36(4), 1135-1144.

Zhou, Y., He, J., Oimahmadov, I., Gadoev, M., Pan, Z., Wang, W., et al. (2016). Present-day crustal motion around the Pamir Plateau from GPS measurements. Gondwana Research, 35, 144-154.